Check for updates

Quantum Confinement in Aligned Zigzag "Pseudo-Ribbons" Embedded in Graphene on Ni(100)

Alessandro Sala,* Zhiyu Zou, Virginia Carnevali, Mirco Panighel, Francesca Genuzio, Tevfik O. Menteş, Andrea Locatelli, Cinzia Cepek, Maria Peressi,* Giovanni Comelli, and Cristina Africh

Lateral quantum confinement is of great interest in tuning the electronic properties of graphene-based nanostructures, making them suitable for technological applications. In principle, these properties might be controlled through the edge topology: for example, zigzag nanoribbons are predicted to have spin-polarized edge states. The practical realization of these structures is of utmost importance in fully harnessing the electronic properties of graphene. Here, the formation of regular, 1.4 nm wide ribbon-like graphene structures with zigzag edges are reported, showing 1D electronic states. It is found that these "pseudo-ribbons" embedded in single-layer graphene supported on Ni(100) can spontaneously form upon carbon segregation underneath 1D graphene moiré domains, extending hundreds of nanometers in length. On the basis of both microscopy/spectroscopy/diffraction experiments and theoretical simulations, it is shown that these structures, even though seamlessly incorporated in a matrix of strongly interacting graphene, exhibit electronic properties closely resembling those of zigzag nanoribbons.

1. Introduction

Lateral confinement is one of the prominent strategies for tailoring the electronic properties of graphene and other 2D materials.[1–3] The most typical example of such 1D quantum confinement is the graphene nanoribbon (GNR), where the nanometer width leads to the opening of an electronic bandgap[4,5] and to the formation of spin polarized edge states.[6] Nonetheless, physical edges are not the only factor leading to 1D electronic states. It has been demonstrated that graphene wrinkles, i.e., 1D bent graphene structures, exhibit many of the electronic properties found in armchair (AC) GNR,[7] e.g., bandgap opening and edge states,[8] while remaining part of a continuous 2D graphene sheet grown on Ni(111). A similar configuration is obtained also in a graphene sheet on the sidewall facet of a SiC substrate.[9,10] In both cases, the key factor for 1D confinement is a ribbon-shaped lifting of graphene from a strongly interacting substrate. Thus, the removal of the graphene–substrate bond in the lifted stripe produces a narrow 1D graphene stripe with charge neutral π-bands embedded in a 2D sheet with π-bands heavily hybridized with the substrate. Such 1D features in 2D materials display very desirable structural properties, e.g., precise alignment of the edges with respect to the substrate, width in the nanometer range, and lack of chemical defects that could hinder the carrier mobility.[7,11] On the other hand, both structures are by construction delimited only by AC edges.

Along these lines, in this work we take a step forward, and demonstrate the formation of 1D ribbon-like structures with zigzag (ZZ) edges, which will refer to as graphene "pseudo-ribbons" (GPRs), embedded in a continuous single-layer graphene sheet. Quantum confinement along ZZ edges is of particular interest because of the predicted spin polarization of the localized edge states,[12–16] a quality that is fundamental for future graphene-based spintronic devices. Our formation method is based on the controlled segregation of carbon atoms patterned by the 1D moiré reported for strongly interacting graphene on Ni(100).[17] The characterization of the morphology and electronic properties of these 1D stripes of noninteracting graphene, enclosed within a continuous, interacting 2D sheet, is experimentally accomplished by a comprehensive

A. Sala, Z. Zou,[+] M. Panighel, C. Cepek, G. Comelli, C. Africh
CNR-IOM Materials Foundry
S. S. 14 km 163.5, Trieste I-34149, Italy
E-mail: sala@iom.cnr.it
A. Sala, V. Carnevali,[++] M. Peressi, G. Comelli
Department of Physics
University of Trieste
Via Valerio 2, Trieste I-34127, Italy
E-mail: peressi@units.it
F. Genuzio, T. O. Menteş, A. Locatelli
Elettra Sincrotrone Trieste
S. S. 14 km 163.5, Trieste I-34149, Italy

The ORCID identification number(s) for the author(s) of this article can be found under https://doi.org/10.1002/adfm.202105844.

[+]Present address: Shanghai Institute of Ceramics, Chinese Academy of Science, Shanghai 200050, P. R. China
[++]Present address: Department of Physics and Science of Advanced Materials Program, Central Michigan University, Mt. Pleasant, MI 48859, USA

ADVANCED
SCIENCE NEWS

www.advancedsciencenews.com

ADVANCED
FUNCTIONAL
MATERIALS

www.afm-journal.de

approach combining surface microscopy at nanometer scale with spectroscopy and diffraction (see the Experimental Section). The experimental findings are corroborated by ab initio theoretical simulations.

2. Results

2.1. GPR Morphology and Atomistic Model

Graphene was grown on Ni(100) by chemical vapor deposition (CVD) on the basis of well-established recipes,[18] resulting in the previously reported 1D moiré pattern.[17] Such pattern raises when one graphene 2D lattice vector lines up with the [011] or [01$\bar{1}$] direction of the substrate, leading to a 1D wave-like height modulation along the AC direction, with a lateral periodicity of ≈1.5 nm. Upon slow cooling of this system to room temperature (≈1 K s^{-1} or less), bulk-dissolved carbon is expected to segregate back to the surface, as previously observed on Ni(111), where it gathers in large amounts at the interface.[19] Scanning tunneling microscopy (STM) topographic images (**Figure 1**a,b) show that the wavy 1D structure of graphene moiré is often interrupted by bright parallel stripes, which cross the whole observed area from side to side, reaching several hundreds of nm in length while maintaining a width of about 1.4 nm. Atomically resolved images (Figure 1c) reveal that such structures are 1D stripes limited by ZZ edges and embedded in the continuous 2D graphene sheet, forming a GPR with typical width of eight ZZ lines, as highlighted by the overlaid model. The registry with respect to the moiré suggests that GPRs are delimited by two next-nearest troughs of the pristine wavy 1D structure, in agreement with the observed width. GPRs with 2.1 nm width, corresponding to the lifting of two consecutive troughs, are only rarely observed and have always a much shorter length. The chemical nature of GPRs is revealed by the selected-area X-ray photoemission spectroscopy (μXPS) of the as-prepared surface, shown in Figure 1d. The C 1s peak presents not only the contribution associated with strongly interacting (n-doped) graphene on clean Ni(100) (in blue), but also a significant component of noninteracting graphene (in green) and two less intense components at lower binding energy (BE), assigned to isolated C atoms dissolved into the Ni bulk (in cyan) and to nickel carbide at the interface (in purple), as previously observed for graphene grown on Ni(111).[18,20] Annealing above the carbide decomposition temperature demonstrates the link between the noninteracting component, the interfacial nickel carbide and the ZZ-GPRs: at 700 K only the strongly interacting graphene component remains (see Figure S1 in the Supporting Information), while low-energy electron diffraction (LEED) pattern shows that the blurring effect induced on the pristine 1D moiré spots by the presence of ZZ-GPRs disappears (see Figure S2 in the Supporting Information). Therefore, it is logical to assume that ZZ-GPRs are made of noninteracting graphene and that their formation is related to the presence of carbon segregated underneath. Upon annealing, ZZ-GPRs disappear as the carbide underneath dissolves into the bulk. This finding is in agreement with STM topography of graphene grown on the (100) face of polycrystalline Ni foils, where no GPR was observed at high temperature.[21] Thus, starting

from the atomistic model of graphene/Ni(100) with 1D moiré presented in Figure 1e,[17] we propose to place carbon atoms under two adjacent moiré periods in the form of interfacial surface carbide (Ni_2C) involving a $c(2 \times 2)$ clock reconstruction of the topmost Ni layer.[22,23] This interfacial carbon deactivates the strong electronic interaction previously existing between the graphene C atoms at the trough of one moiré wiggle and the Ni atoms, breaking the hybridization between carbon p_z-states and nickel d-states and locally restoring the quasi-freestanding nature of graphene.[24] As a consequence, graphene is lifted up, forming the GPR modeled in Figure 1f, whose width is quantized by the pristine moiré lateral periodicity. The atomic arrangement assumed for the nickel carbide at the interface is supported by the double periodicity detected by the intensity line profile of STM topography in Figure 1c at the edges of the GPR, i.e., where the interaction with the atoms at the interface is stronger. The lifting effect of Ni_2C at the interface is confirmed by theoretical density functional theory (DFT) calculations based on the model presented above, which, after relaxation, show that the presence of carbide increases the graphene–Ni distance from 1.9 to 3.3 Å. The overall cell structure in real space and its dual in reciprocal space are depicted in Figure S3a in the Supporting Information. The constant-current STM image built from the proposed atomic model and simulated for a corresponding bias of −0.3 V (shown in Figure 1g), is in very good agreement with the experimental STM image shown in Figure 1c, thus strongly corroborating our interpretation. The noninteracting, quasi-freestanding 1D nature of the ZZ-GPR is further confirmed by the calculated local band structure of the graphene–substrate system. By considering only the contribution of the lifted area of the ZZ-GPR of the supercell along the Γ−K−M direction, a restored Dirac-like π-band that crosses the K point at the Fermi energy (FE) is obtained (Figure 1h, left panel). The band structure projected over the central region of ZZ-GPR is impressively equal in many details to that of freestanding graphene calculated using the same supercell (Figure 1h, right panel). The small blurriness of the first is due to the projection on a subset of atoms instead of plotting the entire band structure and to a nonperfect folding of the graphene K points into the supercell (Figure S3a, Supporting Information). In particular, it should be noted that the Fermi velocity of GPR is predicted to be exactly the same of freestanding graphene. Conversely, the calculated band structure of graphene on clean Ni(100) shows no traces of the unperturbed Dirac cones (Figure S3b, Supporting Information), in analogy with the case of graphene on Ni(111).[20] The GPR thus appears to be a noninteracting, quasi-freestanding 1D graphene stripe delimited by ZZ edges and embedded in a continuous, elsewhere interacting 2D graphene on Ni(100).

2.2. Electronic Properties and 1D Electron Confinement

In order to assess the electronic structure of ZZ-GPR and compare it with ZZ-GNR, we used scanning tunneling spectroscopy, acquiring constant height dI/dV maps. **Figure 2**a (top central panel) shows a map measured at small bias (−0.2 V) from a region including a ZZ-GPR and one 1D moiré wiggle of graphene on Ni(100). The image does not reveal a significant
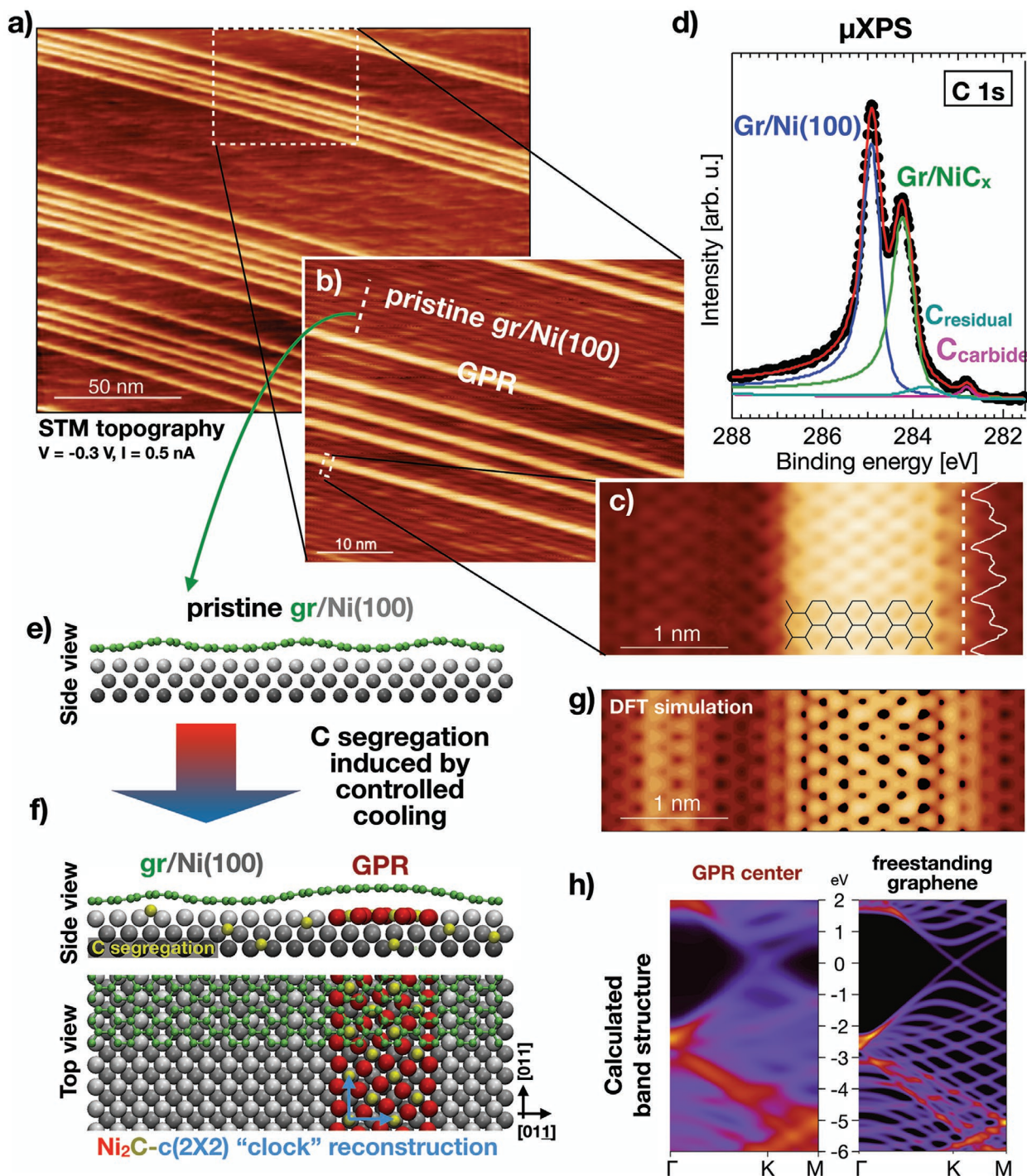
Figure 1. Atomic structure and model of a graphene "pseudo-ribbon" with zigzag edges (ZZ-GPR). a–c) STM topographic images of a single-layer graphene sheet grown on Ni(100) at 830 K after cooling to room temperature, acquired on a large terrace of graphene characterized by the previously reported 1D s-moiré pattern.[17] Long bright parallel stripes, corresponding to GPRs, extend uninterruptedly across the region while maintaining the width of two moiré wiggles. Atomically resolved zoom obtained with a functionalized tip reveals the ZZ edge topology of these structures; the hexagonal texture of graphene is superposed to guide the eye. Along the edges of the ZZ-GPR, the intensity line profile highlights the presence of a periodicity that doubles the graphene lattice vector. STM parameters: $V = -0.3$ V, $I = 0.5$ nA. d) μXPS C 1s spectrum of the as-prepared surface. The peak deconvolution shows that carbon atoms in graphene are affected by two different chemical environments (in blue and green, respectively) and that there are traces of carbon atoms diluted into the bulk ($C_{residual}$, in cyan) and segregated at the graphene/substrate interface ($C_{carbide}$, in purple). e,f) Side and top view of the model structure of the ZZ-GPR with a surface nickel carbide (Ni_2C) under the graphene, exhibiting a $c(2 \times 2)$ "clock" reconstruction. The color code of the atoms is indicated in the taglines. g) DFT simulated constant-current STM image of the model structure at -0.3 V bias. h) Calculated band structures along Γ–K–M of the central atoms of ZZ-GPR (left) and free-standing graphene (right), using the same supercell. See Figure S3 in the Supporting Information for the k-point labeling. The vertical axis expresses $E - E_F$ (eV).
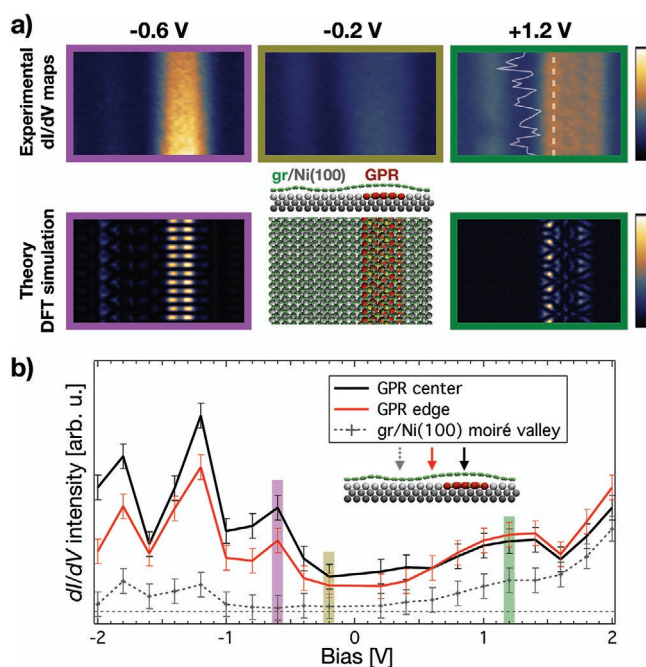
Figure 2. GPR electronic structure by STS and DFT. a) Top panels: Constant-height experimental dI/dV maps of the same region as in Figure 1c, featuring a GPR and a 1D moiré wiggle of graphene on Ni(100) (side and top view models below the central panel), measured at three different biases (−0.6, −0.2, and +1.2 V). dI/dV maps were acquired with a nonfunctionalized, metallic tip. On the experimental map at +1.2 V, the intensity line profile along the dashed line is superposed to highlight the periodicity induced by the (2 × 2) supercell of the carbide underneath. Left and right bottom panels: Simulated spatial distribution of the Kohn–Sham orbitals of the model system, built with electrons with **k** vector close to the K point in the supercell FBZ and energies of −0.6 and +1.2 eV. b) Experimental dI/dV map intensities extracted from selected areas (black: GPR center; red: GPR edge; dashed gray: 1D moiré valley of gr/Ni(100)), extracted from the stack of dI/dV maps taken at several bias values between −2.0 and +2.0 V (not shown). The bars colored in violet, dark yellow, and green highlight the points extracted from the corresponding maps displayed in panel (a). The dashed horizontal line represents the zero value.

enhancement of the local electronic density of states (DOS) in the ZZ-GPR with respect to the rest of the sheet; the small visible contrast is mainly morphological, i.e., it results from the different tip–graphene distances across the area. Conversely, maps measured at −0.6 and +1.2 V biases (Figure 2a, top side panels) show a strong DOS localized on the ZZ-GPR, while the rest of the interacting graphene sheet on clean Ni(100) remains mostly unchanged. The latter maps can be compared to the spatial distribution of Kohn–Sham (KS) orbitals obtained from a DFT simulation of the same area (Figure 2a, bottom side panels). In the relevant energy ranges (−0.6 and +1.2 eV with respect to E_F) and spanning over different **k** points, we have selected wavefunctions showing a large contribution from the C atoms at the edges of the ZZ-GPR, and we show here the plot at constant height of a specific $|\psi_{nk}(\mathbf{r})|^2$. Considering the limited spatial resolution of the experimental dI/dV maps extracted with a nonfunctionalized tip to avoid spurious effects, the agreement is fair. It should be noted that the experimental map at positive bias displays an electronic state localized at the

edges of the ZZ-GPR, similarly to what reported for ZZ-GNRs of comparable width.[25] Here, the intensity asymmetry can be explained by the different registry between the graphene C atoms at the two edges and the surface Ni atoms underneath, as visible in the model in Figure 1f. In addition, both the experimental and KS maps show an edge state with a periodicity along the stripe that doubles the Ni(100) surface vector, thus confirming the presence of Ni$_2$C(100)-(2 × 2) underneath.

STS measurements can also give information on how the local DOS depends on the electron binding energy. To this purpose, a stack of STS dI/dV maps at different biases was acquired, spanning between −2.0 and +2.0 V in 0.2 V steps. From this set, it is possible to plot the dI/dV intensity, measured at constant height, as a function of the bias and for specific regions of interest, e.g., at the center and at the side of the ZZ-GPR, as well as on the 1D moiré valley of graphene on the bare Ni(100) substrate (Figure 2b). This graph suggests the presence of two states around E_F; an occupied state at −0.6 V and an unoccupied, broader state, which has the onset at about +0.8 V and extends up to +1.4 V. As seen in the dI/dV maps, such states are mainly localized in the lifted GPR; in addition, the unoccupied state develops mainly at the edges of the ZZ-GPR and is more intense than the base contribution of interacting graphene on bare Ni(100). Remarkably, the energy split between them is ≈1.4 eV, which is comparable to the energy gap measured on a real ZZ-GNR with similar morphology and size: for a GNR 6 carbon ZZ lines wide, Ruffieux et al.[25] reported an experimental gap of 1.5 eV and a theoretical value of 1.4 eV, respectively. The dI/dV spectrum can also be qualitatively compared with the DOS calculated by DFT simulations, projected onto the carbon atoms for specific regions of interest (the same of Figure 2b) and then rescaled by e^{-2kd} to compensate the variation in the tip-sample distance d for different regions (see Figure S4 in the Supporting Information). The resulting spectra show one peak at −0.6 eV (occupied state) and a broad region of intense DOS centered at ≈+1.0 eV (unoccupied states). The latter unoccupied state is more evident in the spectrum obtained from ZZ-GPR edge (in red), as shown by dI/dV maps. In the projected DOS extracted from the moiré-modulated graphene on clean Ni(100), displayed as dotted line for comparison, the peak at −0.6 eV is not present, while the unoccupied states show only a peak at ≈+0.6 eV that cannot be responsible for the entire broad peak centered at +1.0 V obtained for the ZZ-GPR. Some caveats are necessary when comparing the experimental and theoretical spectra: i) the tunneling current does not probe properly the projected DOS and ii) the rescaling of the latter with the distance of the tip from the probed atoms has been made empirically. Moreover, the energy position of ZZ-GPR cannot be accurately calculated by DFT—it is difficult to obtain a good accuracy in the calculated projection of Bloch states onto atomic-based Bloch sums (sampling over many k points would be needed). Nonetheless, a qualitative agreement clearly emerges between experiment and theory. In addition, the projected DOS for C atoms placed at the edges of the GPR and resolved over the k-space clearly shows the appearance of states with flat dispersion around Γ (see Figure S5a in the Supporting Information), similarly to what happens for ZZ-GNR of comparable width (Figure S5b, Supporting Information). All findings strongly support the picture
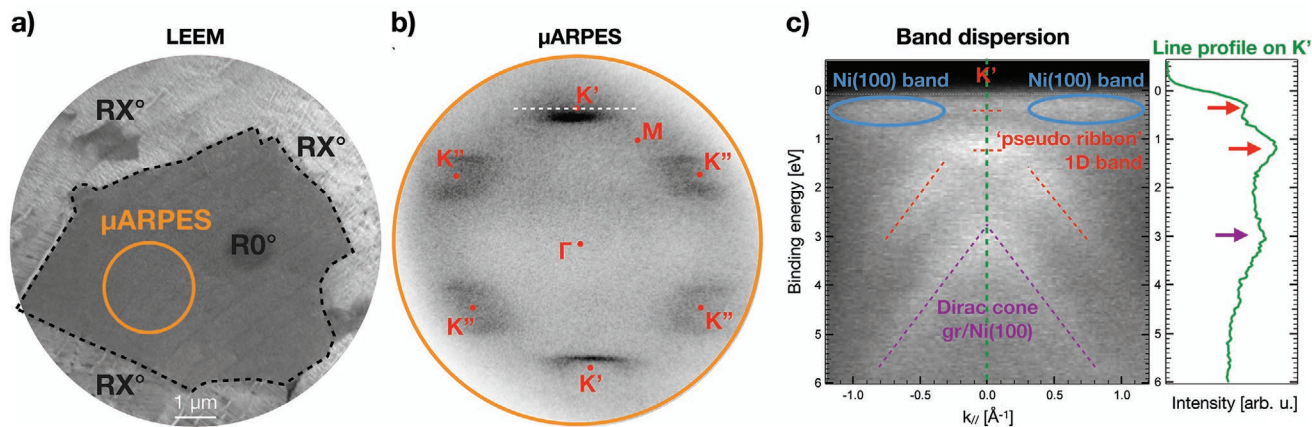
Figure 3. Band structure of a single flake of graphene on Ni(100) including GPR. a) LEEM image of the investigated graphene single flake. Outside the flake border, enclosed in a black dashed contour, other graphene flakes with different rotational angles are imaged. The notation follows ref. [17]: R0° is graphene with 1D moiré and GPR, RX° labels graphene with 2D lattice vectors rotated with respect to the substrate. The homogeneous area contributing to the μARPES map is highlighted in orange. The LEEM image is formed by backscattered electrons with kinetic energy of 9 eV. b) μARPES map (inverted colors) at 1.5 eV binding energy. Photon energy is 40 eV. The high symmetry points Γ, K, and M are marked in red. Because of the 1D character of GPR, the K points can be distinguished in two inequivalent groups, labeled as K′ and K″. c) Momentum distribution curve obtained from the intensity line profiles over a stack of μARPES maps along the line perpendicular to the Γ–K symmetry axis and centered on K (white dashed line in panel (b)). The Ni(100) band is highlighted with blue ovals, while the purple and red lines guide the eye to the branches associated to graphene on clean Ni(100) and 1D GPR, respectively. The intensity line profile of the momentum distribution curve extracted from the vertical, green dashed line is displayed on the right; red and purple arrows highlight the states discussed in the main text.

that electrons in the ZZ-GPR are subject to lateral confinement, even if the 1D structure is embedded in a continuous 2D material. As in the case of wrinkles[7] or folded graphene structures at the edge of a real ZZ-GNR,[26] the fundamental ingredient for the 1D electron confinement appears to be the enclosure of a noninteracting stripe between two strongly interacting areas at the sides, rather than the presence of physical edges as in real GNR. Furthermore, the quantitative agreement between the probed DOS of ZZ-GPR and comparable measurements and calculation carried out on ZZ-GNR of similar size seems to indicate that their electronic structure is indeed analogous.

2.3. Electronic Structure of GPR in Reciprocal Space

The formation of 1D structures naturally aligned with the substrate on a mesoscopic scale offers the rare possibility to investigate the electronic band dispersion of ZZ-GPR by probing the angular distribution of electrons photoemitted from a few-micrometers-wide region (**Figure 3**a). From such area, the energy-filtered angle-resolved photoemission spectroscopy (μARPES) pattern was collected using the Spectroscopic photoemission and low energy electron microscope (SPELEEM), which is capable of mapping the entire 2π angle at once for a selected electron kinetic energy.[27] Figure 3b shows the experimental μARPES map of graphene/Ni(100) including ZZ-GPR due to the presence of nickel carbide at the interface, collected at a BE of 1.5 eV. Band features reminiscent of graphene Dirac cones are clearly visible at the K points, with a pronounced elongation in the horizontal axis. In order to visualize the electronic band structure, the intensity profile measured along the direction marked in Figure 3b is plotted as a function of electron kinetic energy. The result in Figure 3c shows three main contributions: i) the Ni(100) band (in blue), located at the sides

of the K point; ii) a Dirac cone (in purple) centered on K with the Dirac point located at 2.74 ± 0.10 eV BE, corresponding to the strongly interacting 2D graphene on clean Ni(100); iii) another rather peculiar linearly dispersing band feature (in red) at low BE, again symmetric around K and tentatively associated to the Dirac cone of the noninteracting ZZ-GPR, as its linear dispersion and Fermi velocity at higher binding energy is consistent with that of noninteracting graphene.

The peculiar appearance of the latter feature in the ARPES map can be justified with the influence of 1D electron confinement on the angular distribution of photoemitted electrons. The effect of random structural variations on the broadening of graphene Dirac cones has been studied on suspended graphene membranes.[28] At variance with the isotropic broadening observed in random wrinkles in the suspended membranes, the structure factor of 1D ZZ-GPRs is expected to cause a highly anisotropic broadening. In other words, 1D confinement over a certain direction in real space should add broadening exclusively in the corresponding direction of the reciprocal space, thus smearing the band features visible in the ARPES maps only in that direction. The lateral width of the broadening should correspond to the reciprocal of the lateral size of the 1D structures. As a result of this unidirectional broadening, the six K points in graphene first Brillouin zone (FBZ) are not symmetrically equivalent anymore, because the smearing acts along different directions. This effect is explained in detail in the Supporting Information: Figure S6 presents a simulation of the effect of 1D lateral confinement on the Dirac cones of noninteracting graphene in ARPES maps. Figure S6b in the Supporting Information well reproduces the band features observed in Figure 3b, giving support to their origin as due to the ZZ-GPRs.

At very low BE, the electronic states suffer a depletion, leaving only a weak state close to the Fermi energy (BE ≈ 0.4 eV)

and a second state at ≈1.2 eV, which disperses to different $k_{\parallel}$ and gradually assumes the usual Dirac cone shape before 2 eV (Figure 3c). Such states are clearly visible on the linear scan of the plot intensity around K, displayed on the side. By considering the limited experimental energy resolution, these results fairly agree with the dI/dV spectrum presented in Figure 2b, where the filled electronic states show a first peak at bias –0.6 V and a more extended DOS structure at bias lower than –1.2 V.

The incoherent superposition of two graphene π-bands from interacting and noninteracting areas observed here is similar to that reported for rotated graphene grown on Ni(111) and partially lifted by an interfacial layer of nickel carbide, with the significant difference that in that case the lifted areas are 2D and thus the Dirac cones retain the original symmetry.[20] Notably, for Ni(111) the lifting mechanism with nickel carbide intercalation is reversible upon cooling/annealing. The same mechanism appears to work also on Ni(100), but limited to the ZZ-GPR regions: the ARPES maps measured at 700 K and the relative momentum distribution curve around K point, both visible in Figure S7 in the Supporting Information, show that only the heavily n-doped π-bands of graphene on clean nickel, characterized by the classic sixfold symmetry, remain. No trace of the Dirac cone flattened at low BE is visible, confirming that such feature is indeed associated with the presence of ZZ-GPR, as discussed above. Subsequent cooling at room temperature recreates the interfacial nickel carbide, restoring the ZZ-GPRs and bringing graphene back to the mixed configuration. This behavior consolidates the cause–effect relation between carbon segregation and induction of 1D states on graphene. Moreover, by controlling the segregation rate via the preparation parameters one can potentially control the amount of interfacial carbon and therefore the ZZ-GPR density, thus establishing a thermal switch that in principle could be exploited for smart construction of model devices.

3. Conclusions

In summary, it has been demonstrated that the combination of 1D moiré pattern and selective formation of interfacial nickel carbide induces the creation of 1D structures, incorporated in a continuous 2D, single-layer graphene sheet on Ni(100) and behaving like "pseudo-ribbons." Such GPRs are hundreds of nanometers long and only ≈1.4 nm wide, perfectly aligned with one substrate lattice vector and with edges exhibiting ZZ topology. STM-STS data and DFT calculations show that their electronic structure is peculiar, resembling that of quasi-freestanding graphene while the rest of the 2D layer corresponds to graphene heavily interacting with the Ni(100) substrate. In particular, DFT calculations show that the ZZ-GPRs are expected to have very high carrier mobility, as the Fermi velocity coincides with the one of freestanding graphene. The lateral size of the ribbon is determined by the wavy character of the 1D moiré pattern and thus is naturally quantized; the resulting 1D lateral confinement in the ZZ-GPR induces localized states in the electronic structure, whose calculated flat dispersion of the edge states over the k-space is comparable with the bandgap states found for ZZ graphene nanoribbons of similar width fabricated via state-of-the-art bottom-up growth. ARPES data reveal 1D hybridization of the GPR band structure, which

derives from both geometric considerations (the 1D character lifts the original sixfold symmetry of the FBZ, inducing broadening along only one reciprocal space direction) and intrinsic electronic properties (the π-band dispersion is affected by the lateral confinement of the electrons). Importantly, this system constitutes a topical example in which 1D electronic states are present within a continuous 2D film and looks promising for the exploitation of 1D characteristics. The GPRs with ZZ edges are expected to behave like nanowires with enhanced charge/spin transport properties, thus inducing anisotropic electronic characteristic. Their uniform width over lengths of hundreds of nm makes them suitable for model devices at the mesoscopic scale. Moreover, their macroscopic alignment can be easily driven by acting on the nickel substrate. The system could also act as a template to create aligned 1D heterostructures over hundreds of nanometers via deposition of, e.g., metals (creation of nanowires) or molecules (1D framework), offering the unrivalled advantage of having at disposal long stripes with different electronic properties at the nanometer scale.

4. Experimental Section

Sample Preparation: The Ni(100) surface was cleaned by repeated cycles of Ar$^+$ sputtering at 1.5 keV and annealing at 870 K for 5′. The surface cleanness was tested with conventional LEED and XPS. Growth was performed according to the following recipe: the Ni(100) sample was kept at 830 K and exposed to C_2H_4, first at a partial pressure of 5×10^{-6} mbar for 20′, and then at 5×10^{-7} mbar for 180′ in order to slow down the formation of graphene and enhance the amount of carbon diluted into the bulk. Upon slow cooling, in the 680–580 K range, the coexistence of the $c(2 \times 2)$ pattern from Ni_2C and the graphene spots with moiré, as in ref. [17], was clearly recognizable by LEED.

STM Measurements: STM experiments were carried out using an Omicron low-temperature STM (LT-STM), capable of microscopy and spectroscopy measurements at 5 K and at a base pressure below 7×10^{-11} mbar. dI/dV measurements were performed with a lock-in amplifier set at a frequency of 980 Hz and a bias modulation of 16 mV. The experimental system included a standard sample preparation/characterization UHV chamber, equipped with sputter gun, gas line, LEED optics, and fast entry lock.

LEEM/XPEEM Measurements: The cathode lens microscope used for this experiment was the SPELEEM instrument at the Nanospectroscopy beamline at the Elettra synchrotron facility in Trieste, Italy.[27] The electrons photoemitted using the synchrotron beam or generated by an electron gun and backscattered by the sample surface were accelerated by a selected bias and then sent through the microscope lens system, where they could be filtered in energy by a hemispherical electron analyzer, and in real and reciprocal spaces by apertures inserted in specific optical planes. The microscope can selectively display the image plane, the diffraction plane, and the energy dispersive plane on a microchannel plate coupled to a phosphor screen. For the measurements, the LEEM lateral resolution was 10 nm, while the energy resolution was better than 0.35 eV in XPEEM and μARPES, and better than 0.20 eV in μXPS. The circular apertures inserted in an intermediate image plane during diffraction measurements yielded a probed area size with radius 500 nm in μLEED and 2 μm in μARPES and μXPS.

DFT Simulations: DFT calculations were performed with the Quantum ESPRESSO suite of codes,[29] using the plane-wave basis set and generalized gradient approximation for the exchange–correlation functional in the Perdew–Burke–Ernzerhof parametrization (GGA-PBE).[30] For a correct description of graphene–Ni(100) interaction, semiempirical corrections accounting for van der Waals interactions were

2105844 (6 of 8)

included with the DFT-D approach.[31] A kinetic energy cutoff of 30 Ry for the plane-wave basis set was used, as suggested by convergence tests. The equilibrium lattice parameters obtained for the clean Ni(100) surface and for the free-standing graphene were 2.49 and 2.46 Å respectively, in agreement with the experimental values. A periodically repeated slab geometry with 3 Ni layers and graphene adsorbed on one side was used, with a vacuum spacing of 13 Å between graphene and the parallel consecutive Ni(100) surfaces. The in-plane dimensions of the simulation cell were set to 19×2 unit cells of Ni(100), where the factors of 19 and 2 allowed to accommodate respectively an integer number of graphene armchair periods and the Ni_2C-(2×2) structure with clock reconstruction. A Monkhorst–Pack $19 \times 2 \times 1$ k-point grid centered on Γ[32] and the Methfessel–Paxton smearing technique with an energy broadening of 0.01 Ry[33] were adopted for the Brillouin zone sampling. The k-resolved, projected DOS plots were displayed as implemented in Quantum Espresso. Stick-and-ball models were rendered with the VMD software.[34]

Supporting Information

Supporting Information is available from the Wiley Online Library or from the author.

Conflict of Interest

The authors declare no conflict of interest.

Author Contributions

A.S. designed and carried out STM and LEEM/XPEEM measurements, analyzed the data, and drafted the manuscript. Z.Z. and M.Pa. carried out STM measurements. V.C. and M.Pe. performed and analyzed all theoretical calculations. Z.Z., C.C., C.A., F.G., T.O.M., and A.L. carried out LEEM/XPEEM measurements. M.Pe., G.C., and C.A. supervised the project and finalized the manuscript. C.C. and C.A. conceived the experiment. All authors discussed the results and edited the manuscript.

Data Availability Statement

The data that support the findings of this study are available from the corresponding author upon reasonable request.

[1] K. Nakada, M. Fujita, G. Dresselhaus, M. S. Dresselhaus, *Phys. Rev. B* **1996**, *54*, 17954.

[2] A. H. Castro Neto, F. Guinea, N. M. R. Peres, K. S. Novoselov, A. K. Geim, *Rev. Mod. Phys.* **2009**, *81*, 109.

[3] M. V. Bollinger, J. V. Lauritsen, K. W. Jacobsen, J. K. Nørskov, S. Helveg, F. Besenbacher, *Phys. Rev. Lett.* **2001**, *87*, 196803.

[4] K. Wakabayashi, M. Fujita, H. Ajiki, M. Sigrist, *Phys. Rev. B* **1999**, *59*, 8271.

[5] L. Yang, C.-H. Park, Y.-W. Son, M. L. Cohen, S. G. Louie, *Phys. Rev. Lett.* **2007**, *99*, 186801.

[6] W. Han, R. K. Kawakami, M. Gmitra, J. Fabian, *Nat. Nanotechnol.* **2014**, *9*, 794.

[7] H. Lim, J. Jung, R. S. Ruoff, Y. Kim, *Nat. Commun.* **2015**, *6*, 8601.

[8] L. Liu, W. Xiao, D. Wang, K. Yang, L. Tao, H.-J. Gao, *Appl. Phys. Lett.* **2016**, *109*, 143103.

[9] J. Hicks, A. Tejeda, A. Taleb-Ibrahimi, M. S. Nevius, F. Wang, K. Shepperd, J. Palmer, F. Bertran, P. Le Fèvre, J. Kunc, W. A. de Heer, C. Berger, E. H. Conrad, *Nat. Phys.* **2013**, *9*, 49.

[10] I. Palacio, A. Celis, M. N. Nair, A. Gloter, A. Zobelli, M. Sicot, D. Malterre, M. S. Nevius, W. A. de Heer, C. Berger, E. H. Conrad, A. Taleb-Ibrahimi, A. Tejeda, *Nano Lett.* **2015**, *15*, 182.

[11] J. Hicks, A. Tejeda, A. Taleb-Ibrahimi, M. S. Nevius, F. Wang, K. Shepperd, J. Palmer, F. Bertran, P. Le Fèvre, J. Kunc, W. A. de Heer, C. Berger, E. H. Conrad, *Nat. Phys.* **2012**, *9*, 49.

[12] K. Wakabayashi, M. Sigrist, *Phys. Rev. Lett.* **2000**, *84*, 3390.

[13] K. Wakabayashi, K. Sasaki, T. Nakanishi, T. Enoki, *Sci. Technol. Adv. Mater.* **2010**, *11*, 054504.

[14] K. A. Ritter, J. W. Lyding, *Nat. Mater.* **2009**, *8*, 235.

[15] M. Pan, E. C. Girão, X. Jia, S. Bhaviripudi, Q. Li, J. Kong, V. Meunier, M. S. Dresselhaus, *Nano Lett.* **2012**, *12*, 1928.

[16] P. P. Shinde, O. Gröning, S. Wang, P. Ruffieux, C. A. Pignedoli, R. Fasel, D. Passerone, *Carbon* **2017**, *124*, 123.

[17] Z. Zou, V. Carnevali, M. Jugovac, L. L. Patera, A. Sala, M. Panighel, C. Cepek, G. Soldano, M. M. Mariscal, M. Peressi, C. Comelli, C. Africh, *Carbon* **2018**, *130*, 441.

[18] L. L. Patera, C. Africh, R. S. Weatherup, R. Blume, S. Bhardwaj, C. Castellarin-Cudia, A. Knop-Gericke, R. Schloegl, G. Comelli, S. Hofmann, C. Cepek, *ACS Nano* **2013**, *7*, 7901.

[19] M. Singleton, P. Nash, *Bull. Alloy Phase Diagrams* **1989**, *10*, 121.

[20] C. Africh, C. Cepek, L. L. Patera, G. Zamborlini, P. Genoni, T. O. Menteş, A. Sala, A. Locatelli, G. Comelli, *Sci. Rep.* **2016**, *6*, 19734.

[21] Z. Zou, V. Carnevali, L. L. Patera, M. Jugovac, C. Cepek, M. Peressi, G. Comelli, C. Africh, *Carbon* **2020**, *161*, 528.

[22] C. F. McConville, D. P. Woodruff, S. D. Kevan, M. Weinert, J. W. Davenport, *Phys. Rev. B* **1986**, *34*, 2199.

[23] C. Klink, L. Olesen, F. Besenbacher, I. Stensgaard, E. Laegsgaard, N. D. Lang, *Phys. Rev. Lett.* **1993**, *71*, 4350.

[24] A. Dahal, M. Batzill, *Nanoscale* **2014**, *6*, 2548.

[25] P. Ruffieux, S. Wang, B. Yang, C. Sanchez-Sanchez, J. Liu, T. Dienel, L. Talirz, P. Shinde, C. A. Pignedoli, D. Passerone, T. Dumslaff, X. Feng, K. Müllen, R. Fasel, *Nature* **2016**, *531*, 489.

[26] C. Tao, L. Jiao, O. V. Yazyev, Y.-C. Chen, J. Feng, X. Zhang, R. B. Capaz, J. M. Tour, A. Zettl, S. G. Louie, H. Dai, M. F. Crommie, *Nat. Phys.* **2011**, *7*, 616.

**ADVANCED
SCIENCE NEWS**

www.advancedsciencenews.com

**ADVANCED
FUNCTIONAL
MATERIALS**

www.afm-journal.de

[27] T. O. Menteş, G. Zamborlini, A. Sala, A. Locatelli, *Beilstein J. Nanotechnol.* **2014**, *5*, 1873.

[28] K. R. Knox, A. Locatelli, M. B. Yilmaz, D. Cvetko, T. O. Menteş, M. Á. Niño, P. Kim, A. Morgante, R. M. Osgood, *Phys. Rev. B* **2011**, *84*, 115401.

[29] P. Giannozzi, S. Baroni, N. Bonini, M. Calandra, R. Car, C. Cavazzoni, D. Ceresoli, G. L. Chiarotti, M. Cococcioni, I. Dabo, A. Dal Corso, S. de Gironcoli, S. Fabris, G. Fratesi, R. Gebauer, U. Gerstmann, C. Gougoussis, A. Kokalj, M. Lazzeri, L. Martin-Samos, N. Marzari, F. Mauri, R. Mazzarello, S. Paolini, A. Pasquarello, L. Paulatto, C. Sbraccia, S. Scandolo, G. Sclauzero, A. P. Seitsonen, A. Smogunov, P. Umari, R. M. Wentzcovitch, *J. Phys.: Condens. Matter* **2009**, *21*, 395502.

[30] J. P. Perdew, K. Burke, M. Ernzerhof, *Phys. Rev. Lett.* **1996**, *77*, 3865.

[31] S. Grimme, *Wiley Interdisc. Rev.: Comput. Mol. Sci.* **2011**, *1*, 211.

[32] H. J. Monkhorst, J. D. Pack, *Phys. Rev. B* **1976**, *13*, 5188.

[33] M. Methfessel, A. T. Paxton, *Phys. Rev. B* **1989**, *40*, 3616.

[34] W. Humphrey, A. Dalke, K. Schulten, *J. Mol. Graphics* **1996**, *14*, 33.